

Understanding the nanoscale structure of hexagonal phase lyotropic liquid crystal membranes

Benjamin J. Coscia Douglas L. Gin Richard D. Noble Joe Yelk

Matthew Glaser Xunda Feng Michael R. Shirts

January 8, 2018

1 Introduction

Nanostructured porous membrane materials have become increasingly popular for aqueous separations applications such as desalination and biorefinement because they offer the ability to control pore architecture at the molecular scale, thereby permitting the design of solute-specific separation membranes [1]. One can achieve most membrane-based aqueous separations of small molecules using reverse osmosis (RO) or nanofiltration (NF) [2]. While RO and NF have seen many advances in the past few decades, they are far from perfect separation technologies.

Current commercial RO and NF membranes suffer from limitations inherent to their fabrication. Although scalable, each of these two types of membranes has a degree of stochasticity that makes overcoming the permeability-selectivity tradeoff a challenge. Namely, it is difficult to increase the permeability of a desired molecular or atomic species, while maintaining the same retention of an undesired species [3].

Commercial RO membranes are typically dense thin-film composite (TFC) membranes with a porous support layer and an active layer made of a polymer matrix formed through interfacial polymerization [4]. During interfacial polymerization, a step-growth polymerization reaction occurs at the interface of an aqueous monomer solution that has been soaked into the support layer, and an organic solution of a second monomer. The polymer matrix is dense and highly cross-linked which gives high rejections but low permeability.

NF membranes are typically porous membranes made by a phase-inversion process. The most widely used phase-inversion process is immersion precipitation, during which one submerges a polymer, dissolved in a solvent, in a non-solvent. A solid, porous polymer membrane is all that remains once all solvent has been removed by non-solvent exchange [5]. The resultant pores are polydisperse in size, which hurts membrane

selectivity. A second technique used to create NF membranes is call track-etching in which a polymer film is bombarded with charged particles, then chemically etched to create pores [6]. The pores are uniform, which benefits selectivity; however, the membranes have a low porosity and subsequently low permeability.

The permeability-selectivity tradeoff has the potential to be overcome by designing membranes at the molecular level. Next-generation nanoporous membranes with high selectivity, permitted by a precisely controlled pore size, and high permeability, allowed by its porous architecture, have the potential to replace traditional RO and NF membrane technologies.

Development of nanostructured porous materials has been limited by the ability to synthesize and scale various fundamentally sound technologies. Graphene sheets are atomically thick which results in excellent water permeability but defects during manufacturing severely impact selectivity [7]. Molecular dynamics (MD) simulations of carbon nanotubes show promise [1], but synthetic techniques are unable to achieve scalable alignment and pore monodispersity [8, 9]. Zeolites have sub-nm pores with a narrow pore size distribution, and MD simulations of these materials show that they exhibit complete rejection of solvated ions [10]- however, experimental rejection was low and attributed to interstitial defects formed during membrane synthesis [11]. Consequently, there is a need for a scalable nanostructured porous membrane.

Polymeric membranes based on self-assembling lyotropic liquid crystals (LLCs) are suitable candidates for aqueous separation applications. LLCs are amphiphilic molecules that share the characteristic ability of nanostructured porous membrane materials to create highly ordered nanostructures with the added benefits of low cost and synthetic techniques feasible for large-scale production [12]. LLC systems created by the monomer Na-GA3C11 (Fig. 1a) have been extensively studied experimentally [12, 13, 14, 15, 16]. The neat Na-GA3C11 monomer forms the thermotropic liquid crystalline (TLC) Col_h phase (Fig.1). The presence of ca. 10 wt% added water results in formation of the lyotropic H_{II} phase. In both cases, Na-GA3C11 monomers assembles into mesophases made of hexagonally packed, uniform size, cylinders with hydrophilic head groups oriented inward towards the cylinder center. This LLC assembly is then polymerized in situ to form a cross-linked polymer network to stabilize the structure. The hydrophilic region can act as a pore for aqueous separations [14]. One can envision tailoring the pore region for specific separations by changing the monomer chemistry [15].

Research into polymerized LLC membranes has been revived in recent years. During early stages of exploration, mesophases formed by Na-GA3C11 could not be macroscopically aligned, resulting in low flux membranes, and no clear route towards scalable and economical filtration. In 2014, Feng et al. showed that one can align the mesophases using a magnetic field with subsequent cross-linking to lock the structure in place [12]. In 2016, Feng et al. showed that one could obtain the same result using a second technique termed soft confinement [16].

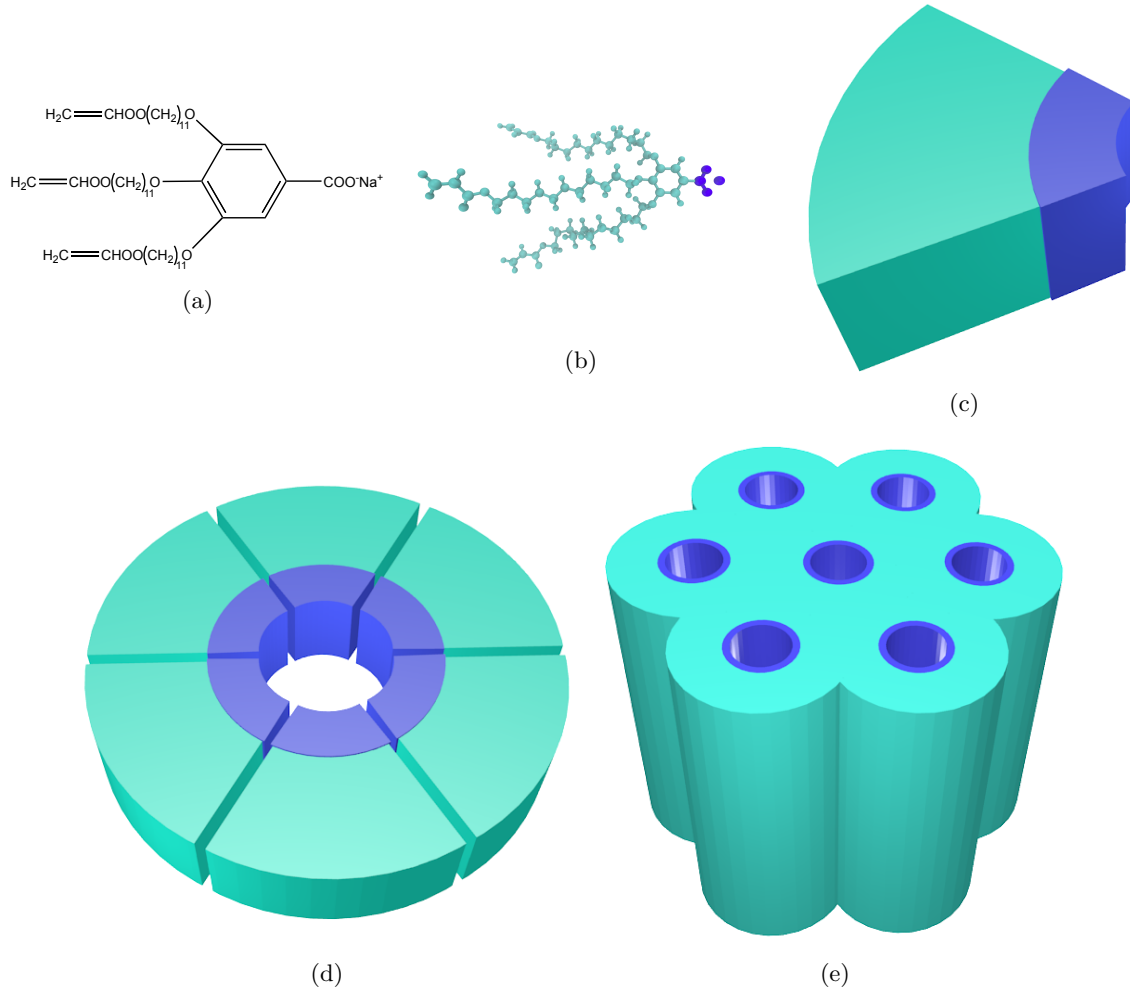


Figure 1: The LLC monomer Na-GA3C11 (a) rendered atomistically (b) exhibits wedge-like character (c). Monomer wedges assemble into disks (d) with hydrophilic head groups (blue) facing towards the disk center. The disks assemble into hexagonally packed columnar mesophases (e).

Our current understanding of LLC systems is not rich enough to be able to precisely design membranes for specific separations. Over the past 20 years, H_{II}-phase LLC polymer membrane studies have been limited primarily to Na-GA3C11 with some characterization done after minor structural modifications. Resel et al. varied the length of the monomer tails and the counterion used and observed its affect on pore spacing [17]. In a later study of rejection performance, it was shown that membranes formed by cross-linked Na-GA3C11 in the H_{II} phase cannot separate solutes less than 1.2 nm in diameter because the pores are too large [14]. We do not yet understand how to controllably reduce the effective pore size or how to tune the chemical environment in the nanopores of this or related materials for effective water desalination and small organic molecule separations. The only source of predictive modeling for LLC systems have been macroscopic models that likely do not adequately describe transport at these length scales [18]. It will be challenging to efficiently narrow down the large design space in a laboratory setting without a robust model.

In this study, we build a significantly more realistic atomistic model of LLC membranes than, to our knowledge, has ever previously been done, and explore what new structural information can be gained and what structure hypotheses are supported by this model. We validate the model using as much experimental information as possible. We are most interested in reproducing the conclusions about structure drawn from small angle X-ray scattering (SAXS) and wide angle X-ray scattering (WAXS) experiments as well as in matching ionic conductivity measurements [16].

A molecular-level understanding of LLC polymer membrane structure, enabled by molecular dynamics simulations, can provide guidelines to reduce the large chemical space available to design monomers for creation of separation-specific membranes. A good molecular model should incorporate a detailed picture of the nanoscopic pore structure which will be crucial to understanding the role of monomer structure in solute transport and membrane design. Models resulting from molecular dynamics simulations will provide the required level of detail (Fig. 2), assuming the force fields are sufficiently accurate. With such an atomistic model, we can directly observe molecular-level solute transport and suggest governing mechanisms. We can observe how the choice of head group may influence pore size for size exclusion driven separations. We can interchange counterions which may influence both the pore size and the strength of the Donnan potential which affects the degree to which the membrane can exclude charged species.

In order to appropriately model transport in these ordered, nanoporous organic systems, we must first gain a thorough understanding of the nanoscopic structure of LLC polymer membranes. Our approach to constructing a general model will follow the development of a model of the assembly formed by Na-GA3C11 since it has sufficient experimental characterization. We have also narrowed our scope to the development of a model of the Col_h phase membrane. Compared to the H_{II} phase, the Col_h phase is a simpler starting point, due to the absence of water, and has detailed experimental wide-angle X-ray scattering (WAXS) patterns

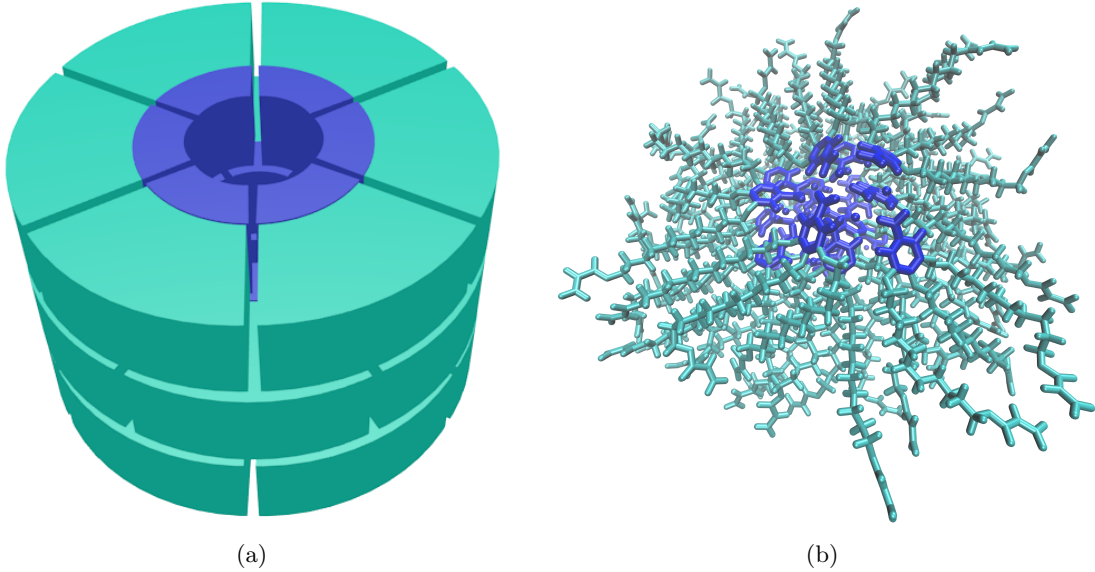


Figure 2: We can only speculate about solute behavior inside the membrane pores based on our previous picture of the pore structure (a). We will use a detailed molecular model in order to appropriately model the pore’s complex architecture which is crucial to understanding the mechanism of solute transport (b). The head group region is colored blue and the tail region is colored cyan in both representations.

useful for reconstructing structural data. The two phases appear to share similar structural characteristics since the pore spacings in each system are in close agreement [16, 17].

Despite having structural data, there is still information which experiment cannot definitively answer. Our current level of understanding suggests that monomers partition into layers with head groups facing towards the center, then stack on top of each other to create pores that pack together hexagonally. There are several key questions that we will investigate in order to expand this understanding:

1. If layers do exist, how many monomers constitute a single layer?

A simple molecular simulation study of a similar molecule suggested that there are 4 monomers in each layer [19]. Their model likely does not sufficiently model the chemical environment present in the real system since it only contains 16 total monomers. A separate calculation based on the estimated volume of the liquid crystal monomers proposes that each layer consists of seven monomers [17]. Our best chance to answer this question is by using a molecular model orders of magnitude larger than any other reported atomistic liquid crystal membrane simulation, as we present here. We will directly change the layer composition and note its effect on membrane structure.

2. Does our model support the existence of layers and if so, how well defined are the layers?

Strong π - π stacking interactions in the direction perpendicular to the membrane plane support the existence of layers experimentally. π - π stacking will only occur between the aromatic monomer head groups which leaves no description of what is happening in the monomer tail region. The tails may entangle isotropically while maintaining stacking order among headgroups.

3. How do monomers in each layer position themselves with respect to surrounding layers?

The π - π stacking interactions may be a driving force of self-assembly in this system [20]. Gas phase ab initio studies of benzene dimers have shown a clear energetic advantage for parallel displaced and T-shaped π - π stacking conformations over a sandwiched conformation [21]. Substituted benzene rings exhibit an even stronger π - π stacking attraction which favors the parallel displaced configuration in all cases except where the substitutions are extremely electron withdrawing. [22, 23] In this study, we compare simulated X-ray diffraction patterns to experiment in order to deduce which stacking configuration is most likely.

4. Can the system exist in other metastable states or phases that are not accessed during experiments?

There remains the possibility that there is more than one metastable state associated with a given LLC phase. Simulating a membrane atomistically requires many atoms which limits the timescales accessible with MD. It is reasonable to expect that we will generate configurations which are kinetically trapped in a metastable free energy basin. We must be able to identify which state is produced experimentally.

5. What constitutes a pore, and how well-defined are the pore regions?

The limited picture that experiment provides tells us that there are hexagonally packed, hydrophilic regions where transport is likely to occur. One may instinctively assume that these regions are tube-like pathways. We will explore the composition of the pores and the partition between the hydrophilic and hydrophobic regions.

6. Is it necessary to include any water in order to appropriately model the Col_h phase?

While past work describes the Col_h phase as dry [12], it has been suggested by experimentalists, in unpublished communications, that it is likely that neat monomer leaches small amounts of ambient water. Experimentally, achieving a hexagonal phase with a completely dry system has proven difficult. If neat monomer sits in ambient conditions, its color turns from transparent to slightly opaque and a hexagonal phase forms. Although we will not explore whether water is necessary for self-assembly, we hypothesize that the hydrogen bonding network formed by the water may play a role in structuring the pores and holding together the hexagonal phase. We can use simulated X-ray diffraction patterns to see if there is any meaningful structural difference between a “dry” and “wet” system.

We used experimental small-angle X-ray scattering (SAXS) data from [16] (Fig. 3a) and wide angle X-ray scattering (WAXS) data (Fig. 3b, produced as described in [12]) for comparison to our model. We rely primarily on the 2D WAXS data since it encodes all structural details down to the sub-nm scale. There are five major features of interest present in the 2D experimental pattern shown in Figure 3b.

1. The location of the first is at $q_z = 1.7 \text{ \AA}^{-1}$, corresponding to a real space separation of 3.7 \AA . Previous work [12] attributes this reflection to π - π stacking between aromatic rings in the direction perpendicular to the membrane plane, or z-axis [12]. For simplicity, we will refer to this reflection as R- π .
2. A weak intensity line, located at exactly half the q_z value of R- π ($q_z = 0.85 \text{ \AA}^{-1}$), corresponds to a real space periodic spacing of 7.4 \AA . This reflection has been interpreted as 2_1 helical ordering of aromatic rings along the z axis [12], meaning that if one traces the positions of the aromatic rings with a helical curve, then for each full turn in the helix, one will encounter two aromatic rings. For this reason we will refer to reflection as R-helix.
3. A low intensity ring located at $r = 1.4 \text{ \AA}^{-1}$ marks the third major reflection of interest. The real space separation corresponds to 4.5 \AA which is characteristic of the average spacing between packed alkane chains [24]. We will call this reflection R-alkanes.
4. Within R-alkanes, are four spots of higher relative intensity. Accordingly, we name these reflection R-spots. The location of all spots is ~ 37 degrees from the q_z axis in their respective quadrants. In many liquid crystal systems one can explain the spots by the tilt angle of the alkane chains with respect to the membrane plane [25].
5. The final feature corresponds to the spacing and symmetry of the d_{100} plane. This plane is geometrically related the distance between pores. The feature, which we named R-pores, is characterized by dots along the equatorial axis defined when $q_z = 0$. The spacing between dots is indicative of the hexagonal symmetry of the packed pores. We observe the same information with higher resolution using SAXS (Fig. 3a).

2 Methods

2.1 Monomer Parameterization

We parameterized the liquid crystal monomers using the Generalized AMBER Force Field [26] with the Antechamber package [27] provided with AmberTools16 [28]. We assigned atomic charges using the am1bccsym

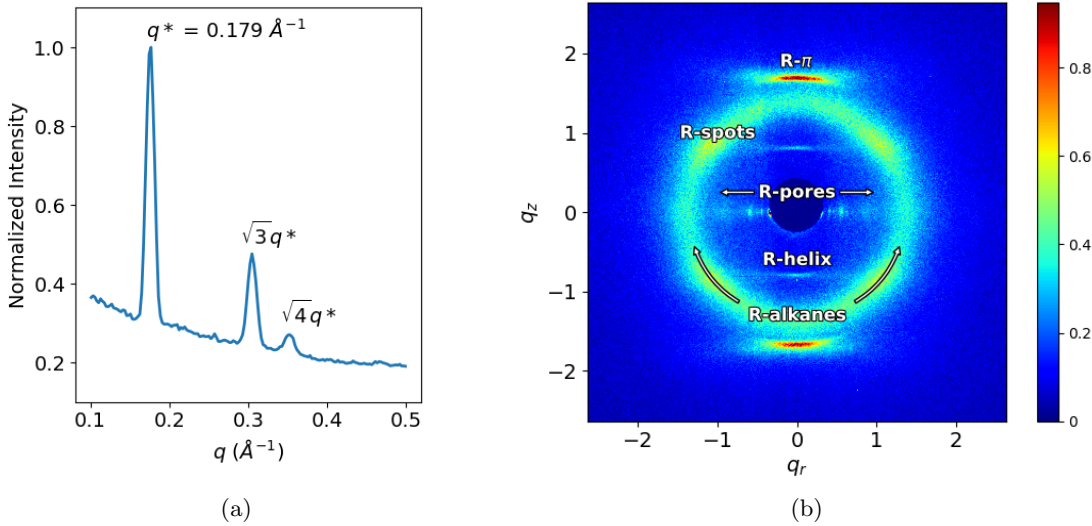


Figure 3: (a) (Reproduced from [16]) The repeat spacing in the 1D small angle X-ray scattering pattern is characteristic of hexagonal packing. The leading peak, q^* , represents the distance between the d_{100} planes. Using this distance, we know that the distance between pore centers is 4.12 nm. (b) 2D WAXS gives details about repeating features on the order of angstroms. Experimentalists have explained each of the 5 major reflections present as follows: (R- π) Aromatic head groups $\pi - \pi$ stack 3.7 Å apart. (R-helix) Monomers arrange vertically in a 2_1 helix. (R-alkanes) Alkane chain tails pack 4.5 Å apart. (R-spots) Monomer tails are tilted with respect to the membrane plane. (V) As derived from SAXS, the pores are spaced 4.12 nm apart and pack hexagonally

method of molcharge shipped with QUACPAC from Openeye Scientific Software. We ran all molecular dynamics simulations using Gromacs 2016 [29, 30, 31, 32].

We generated an ensemble of characteristic, low-energy vacuum monomer configurations by applying a simulated annealing process to a parameterized monomer. We cooled monomers from 1000K to 50K over 10 nanoseconds. We randomly pulled a low energy configuration from the trajectory then reassigned charges using `molcharge`. Using the new charges, we annealed the monomer system again and pulled a random monomer configuration from the trajectory which we used for full system construction (Figure 4a). See supplemental information for further detail.

2.2 Unit Cell Preparation

The timescale for self-assembly of monomers into the hexagonal phase is unknown and likely outside of a reasonable length for an atomistic simulation, calling for a more efficient way to build the system. Previous work has shown a coarse-grained model self assemble into the H_{II} phase configuration in ~1000 ns [33]. We attempted atomistic self-assembly by packing monomers into a box using Packmol [34]. Simulations of greater than 100 ns show no indicators of progress towards an ordered system. To bypass the slow self-assembly process, we use Python scripts to assemble monomers into a structure close to one of a number of

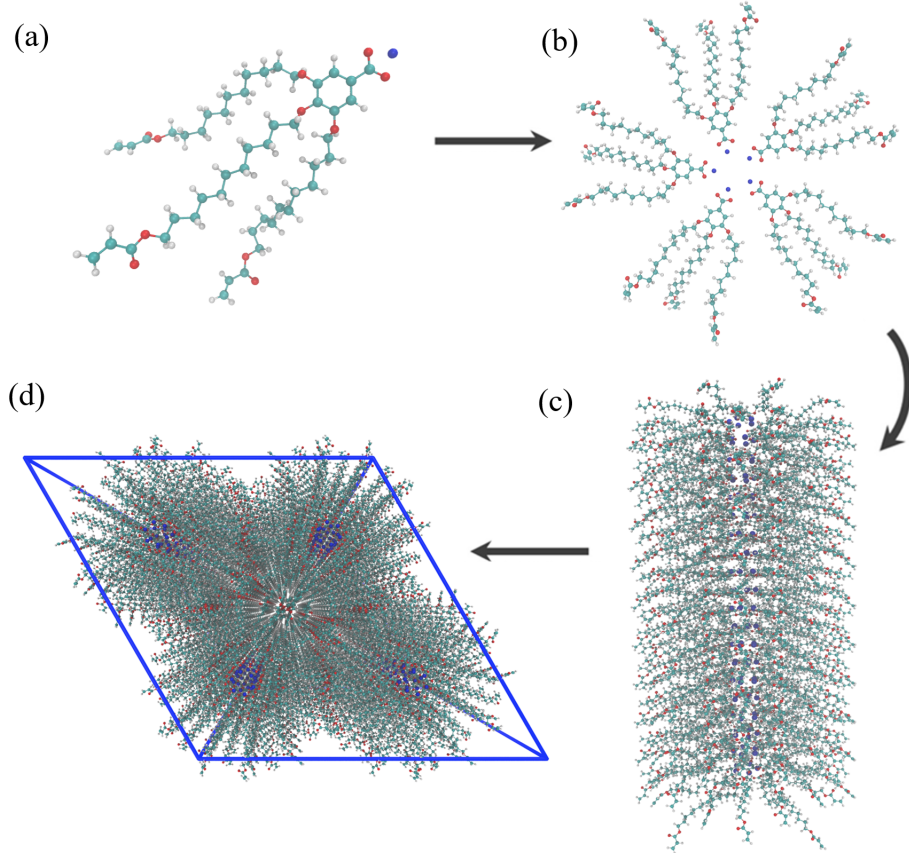


Figure 4: (a) We parameterized a single monomer and annealed it to produce a low energy configuration. (b) A python script rotates and assembles monomers into layers with hydrophilic centers. (c) We chose to stack twenty layers on top of each other to create pores. (d) The pores are duplicated and placed into a monoclinic unit cell

hypothesized equilibrium configurations (Figure 4).

A typical simulation volume contains four pores in a monoclinic unit cell, the smallest unit cell that maintains hexagonal symmetry when extended periodically. Each pore is made of twenty stacked monomer layers with periodic continuity along the pore axis, avoiding any edge effects and creating an infinite length pore ideal for studying transport. We prefer a small number of layers in order to reduce computational cost and to allow us to look at longer timescales. Ultimately, we chose to build a system with 20 monomer layers in each pore in order to obtain sufficient resolution when simulating X-ray diffraction patterns.

2.3 Monomer Placement

When constructing an initial configuration, there are a number of variables which require careful consideration while placing monomers. The equilibrium configuration is sensitive to some while insensitive to others. The starting pore radius, defined as the distance of a chosen head group carbon from the pore's

central axis, does not influence the equilibrium structure if one chooses a reasonable value (See Supplemental Information). The pore radius is chosen to be 0.6 nm in our initial configurations because the pore size is estimated to be \sim 1.2 nm [14]. The initial distance between pores also has little effect on the the equilibrated structure (See supplemental information). However, one should not start them too close or there will be high energy repulsions during early equilibration. We chose an initial pore spacing of 4.5 nm, \sim 10% larger than the experimental value of 4.12 nm. The distance between layers, the rotation of the layers with respect to adjacent layers, and the number of monomers per layer do influence the equilibrium structure and require further justification for their choices. We rely on experimental data to inform them.

We chose the layer spacing for the initial configuration based on $R-\pi$ and then allowed the system to readjust during equilibration. Each monomer was rotated so the plane of the aromatic head groups would be coplanar with the xy plane. We explored three different initial layer spacings. The first is exactly equal to $R-\pi$ with layers placed so aromatic rings stack 3.7 Å apart in the z-direction. We explore a second system with an initial layer spacing of 5 Å. We briefly explored a third system with an initial layer spacing of 10 Å. If we initially space layers too far apart, they will collapse on each other while simultaneously slipping in between layers of adjacent pores, which leads to an artificially thick membrane with pores spaced closely together. Further details of simulations with layer stacked 10 Å apart are in the supplemental information.

We chose the relative interlayer orientation based on clues from diffraction data as well as the various known stacking modes of benzene and substituted benzene rings: sandwiched, parallel-displaced and T-shaped [21] (Fig. ?? and ??). We ruled out the T-shaped configuration because its \sim 5 Å equilibrium stacking distance [21] is inconsistent with $R-\pi$. It is also infeasible for the monomers to orient in the T-shaped conformation because of the bulky tail groups. We will explore the system's preference towards the sandwiched vs. parallel displaced stacking modes in some detail. Both have reported stacking distances near the $R-\pi$ value of 3.7 Å. Headgroups in our sandwiched initial configuration stack directly on top of each other while headgroups in the parallel displaced initial configuration stack with an offset of $180/n_{mon}$ degrees where n_{mon} equals the number of monomers per layer.

The number of monomers in each layer is unknown, as stated in (1). We tested configurations constructed with a varied number of monomers per layer. We built systems in the offset and parallel displaced configurations with 4, 5, 6, 7 and 8 monomers per layer.

2.4 Equilibration

We developed equilibration schemes to create dry and wet configurations. Both schemes start with an initial configuration generated according to the previous guidelines. To create a dry configuration, we fix

monomer head groups in the sandwiched or parallel-displaced configuration using position restraints with a force constant of 10^6 kJ mol $^{-1}$ nm $^{-2}$. We run a 50 ps simulation in the NVT ensemble which allows the monomer tails to settle without disrupting the ordering of the head groups. Doing so also mitigates system dependence on initial monomer configuration. Every 50 ps, we reduce the force constants by the square root of its previous value. Once the force constant is below 10 KJ mol $^{-1}$ nm $^{-2}$, we reduce the restraints in a sequence with values of 8, 3, 2, 1, and 0 KJ mol $^{-1}$ nm $^{-2}$ respectively. We allow the resulting unrestrained structure to equilibrate for 5 ns in the NPT ensemble with pressure controlled by the berendsen barostat. Next, we run long NPT equilibration simulations for at least 400 ns using the Parrinello-Rahman barostat with a time constant of 10 ps.

In order to create a wet system, we solvated an initial configuration with water using `gmx solvate`. We remove all water molecules placed outside the pore region. Then we randomly remove water molecules inside the pore region until the pores reach the desired concentration of water. The remainder of the equilibration follows the same procedure as the dry system.

2.5 Cross-linking

In order to fully match synthetic procedures, we created a cross-linking algorithm that one can apply to equilibrated structures. The purpose of cross-linking is to maintain macroscopic alignment of the crystalline domains, ensuring aligned, hexagonally packed pores. For that reason, we are not concerned with replicating the kinetics of the reaction, but instead emphasize the consistency of the final structure with experimental structural data.

We developed the algorithm based on the known reaction mechanism. Cross-linking of this system is a free radical polymerization (FRP) taking place between terminal vinyl groups present on each of the three monomer tails. FRPs require an initiator which bonds to the system, meaning new atoms are introduced into the system. For simplicity, we simulated the initiator as hydrogen and made it present in the simulation by including them as dummy atoms in all possible locations where an addition could occur. We carry out the cross-linking procedure iteratively. During each iteration, the algorithm selects eligible bonding carbon atoms based on a distance cut-off. The topology is updated with new bonds and dummy hydrogen atoms are changed to appropriate hydrogen types. Head-to-tail addition was the only propagation mode considered due to its dominance in the real system [35]. We did not consider direction of attack because the resultant mixture is racemic.

Our implementation requires long simulation times to achieve high cross-link densities. A typical cross-linking procedure can take up to 24 hours. In order to collect equilibrated data, further NPT simulation is

necessary. We typically run a cross-linked system for an additional 100 ns to allow the system to readjust. For those reasons we did not cross-link all systems tested, but only the most promising structure. We show that cross-linking does not significantly change any of our drawn conclusions in Section 3.6.

2.6 Equilibrium Calculations

Using equilibrated structures, we carry out various calculations to characterize the system. We define the point at which a system is equilibrated based on when the distance between pores stops changing. We determined when the distances stopped changing by applying the statistical test, `pymbar.timeseries.detectEquilibration`, to the time series [36, 37]. Simulations of 400 ns give at least 50 ns of equilibrated simulation trajectory.

To calculate the equilibrated pore spacing, we measured the distance between pore centers. We located the pore centers by averaging the coordinates of sodium ions in their respective pores. We generated pore spacing statistics using the bootstrapping technique (See Supplemental Information).

To quantify the degree of layering and the equilibrium distance between layers in our system, we calculate a spatial correlation function, $g(z)$, measured along the z-axis (perpendicular to the membrane plane). To calculate $g(z)$, we binned the z-component distances between the center of mass of each component and all others of the same pore over at least 50 ns of equilibrated trajectory and then normalized by the average number density. To extract the average distance between layers we applied a discrete Fourier transform to $g(z)$ and extracted the highest intensity frequency.

This section replaced by Yelk/Glaser text. Simulated X-ray diffraction patterns are generated based on atomic coordinates in order to make a direct experimental comparison. All atomic coordinates were simulated as Gaussian spheres of electron density corresponding to each atom's atomic number. A three dimensional Fourier transform (FT) of the array of electron density results in a three dimensional structure factor which represents the unit cell in reciprocal space. We matched experimental 2D WAXS patterns by adjusting the initial spacing between layers and the orientation of the head groups with respect to adjacent layers.

We normalized the colorbars on all diffraction patterns relative to R-alkanes. We believe that the alkane-alkane density, averaged over all angles, is the feature most likely to be replicated between experiment and simulation. Other features are dependent on system ordering which is likely to have some dependence on initial configuration. We calculated the average intensity within R-alkanes of the experimental pattern, I_{avg} . We exclude intensities within $\pm 30^\circ$ of the meridional axis defined by $q_r = 0$, since the simulated patterns differ from experiment in those regions. Specifically, in contrast to the experimental WAXS pattern, R- π appearing in simulated diffraction patterns intersects with R-alkanes (See Fig. 7). We multiplied I_{avg} by a

scaling factor of 2.5. Intensities that appear in the experimental pattern $\geq 2.5I_{avg}$ receive colorbar values of 1. We apply the same scaling method to the simulated patterns. We carefully chose a scaling factor of 2.5 in order to (1) visibly display all features in the experimental pattern and (2) to allow us to compare the relative intensities of features between simulated and experimental diffraction patterns.

We explored the pore composition by measuring the average number densities of various monomer components as a function of distance from the pore centers. We looked at the average number density of sodium ions, aromatic rings and carbon atoms making up the monomer tails. We binned the radial distance of all atoms in each group from the pore centers, then normalized by the volume of the annulus defined by the bin edges and z box vector.

We calculated ionic conductivity using two different methods for robustness. The Nernst-Einstein relation relates the DC ionic conductivity to ion diffusivity, D , concentration, C , ion charge, q , the Boltzmann constant, k_b , and temperature, T :

$$\sigma = \frac{q^2 C D}{k_b T}$$

We measured sodium ion diffusion coefficients by calculating the slope of the linear region of the z-direction mean square displacement curve as indicated by the Einstein relation [38]. We visualized the MSD plot to determine where to begin and end a linear fit. We measured ion concentration with respect to the volume of the entire unit cell.

The second method, termed the Collective Diffusion model, measures the movement of the collective variable, Q , which is defined as the amount of charge transfer through the system and can be thought to represent the center of charge of the system. The conductance, γ , of the system can be calculated as:

$$\gamma = \frac{D_Q}{k_b T}$$

We convert the resulting value to ionic conductivity by multiplying by channel length and dividing by the membrane cross sectional area. D_Q is the diffusion coefficient of the collective variable Q . It is calculated using the Einstein relation. One can access a full derivation of the model elsewhere [39].

3 Results and Discussion

3.1 Determining the Number of Monomers per Layer

Our simulations best support a model built with 5 monomers per layer based on the measured equilibrated pore-to-pore distances. To discern the composition of the monomer layers, addressing (1), we ran simulations

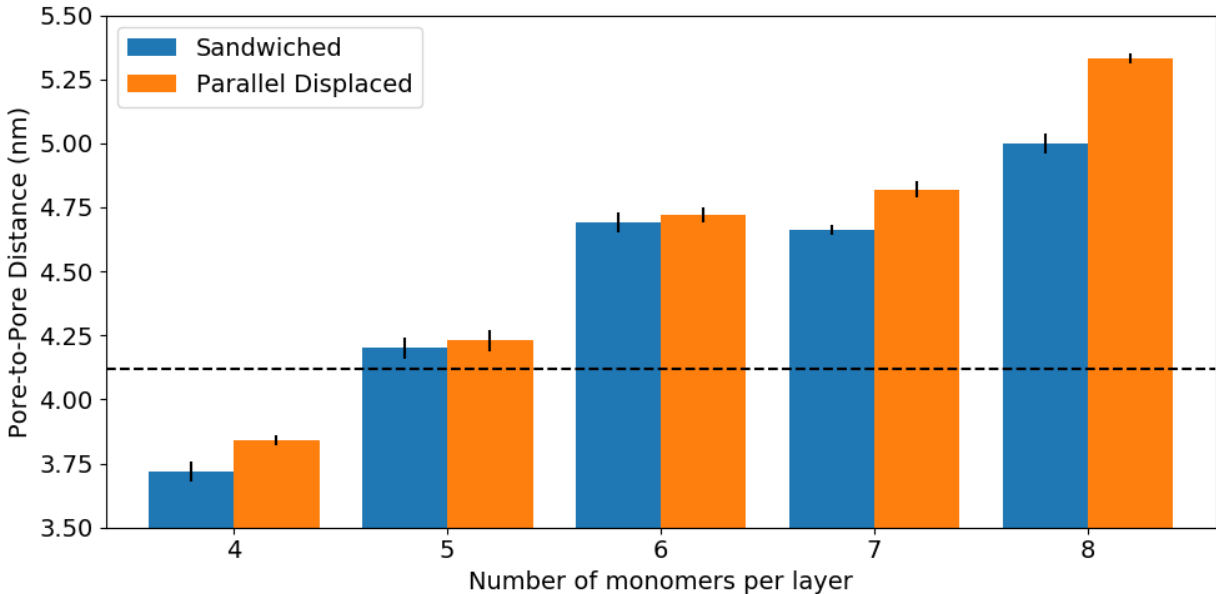


Figure 5: When we build systems with 5 monomers per layer in the parallel displaced configuration, the equilibrated pore spacing is closest to the experimental value of 4.12 nm. The equilibrated pore spacing of the model increases as the number of monomers in each layer increases. The pore spacing of systems starting in the sandwiched configuration is systematically slightly lower than those started in the parallel displaced configuration.

of systems created with 4 - 8 monomers per layer. We built systems in both the parallel displaced and sandwiched configurations with layers initially spaced 3.7 Å apart. We prepared equilibrated configurations according to the dry equilibration procedure. All systems are stable after 400 ns of simulation. In a sense, all systems are at least metastable, addressing (4), however not all will make physical sense or fit the experimental profile that we are looking to match. Figure 5 shows the pore spacing for all systems tested. Systems built with 5 monomers in each layer equilibrate to a pore spacing that is most consistent with the experimental value of 4.12 nm derived from SAXS measurements (Figure 3a). The remainder of this discussion will focus on the analysis of systems built with 5 monomers per layer.

3.2 Determining Definition of Layers

We learned that layers are well-defined and persistent, answering (2). We established our conclusion by plotting the pair correlation function, $g(z)$, calculated between atoms along the length of the pores (Fig. 6). We measured $g(z)$ with respect to aromatic rings in the head groups and, separately, with respect to carbon atoms in the alkane chains. Using a Fourier transform of $g(z)$, we see that sandwiched configuration layers stack 4.39 Å apart while parallel displaced configuration layers stack 4.38 Å apart.

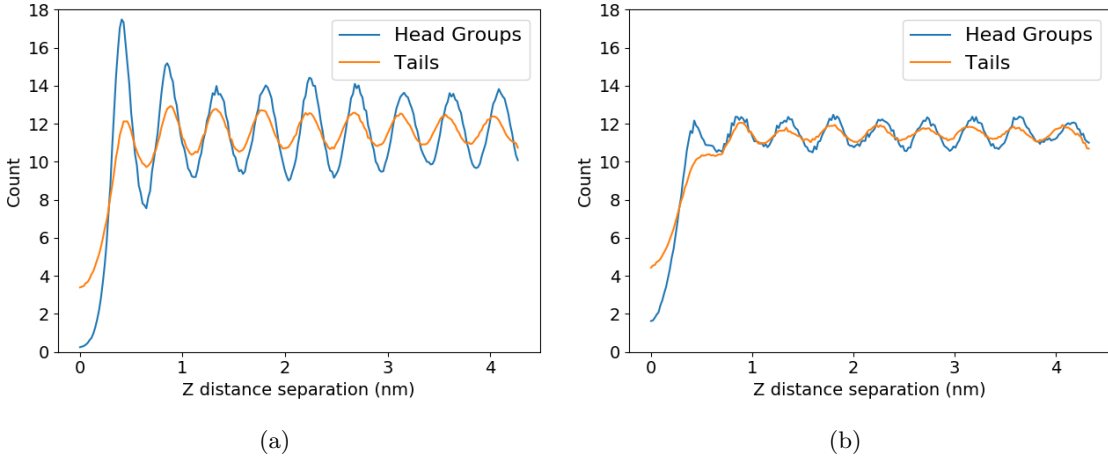


Figure 6: We support the existence of layers with the observance of clear periodic maxima in the z -direction pair distribution functions of the (a) 5 monomer per layer, sandwiched and (b) 5 monomer per layer, parallel displaced configurations. The extent to which we consider a system to be layered is based on the magnitude of the deviation of the periodic maxima from the average number density. The sandwiched configuration possesses a higher degree of layering than the parallel displaced configuration and, in both cases, the head group region has a higher degree of layer partitioning than the tail region. (See supplemental information for detailed definitions of the head group and tail regions)

3.3 Determination of Relative Interlayer Head Group Orientation

We answer question (3) by simulating X-ray diffraction patterns produced from equilibrated MD trajectories. We tested systems built with 5 monomers per layer in the parallel displaced and sandwiched configurations. We generated simulated patterns using portions of simulation trajectory after equilibration. The patterns for both structures are shown and compared to experiment in Figure 7.

Simulated XRD of the sandwiched configuration contains all experimental features except for R-helix. R-alkanes, R-spots and R-pores appear close to their expected locations. R- π is also present, however it intersects R-alkanes at a q_z value lower than experiment meaning the head groups in our model prefer to stack farther apart.

The parallel displaced configuration results in a simulated XRD pattern with the closest match to experiment. It produces the only pattern that exhibits all major reflections. R-alkanes and R-pores appear as they do in the sandwiched configuration. R-spots and R- π appear, however with a lower intensity relative to R-alkanes when compared to the sandwiched configuration. R-helix appears due to the parallel displaced aromatic rings. It is a subharmonic of R- π since the nearest vertically stacked head group to any given head group is 7.4 Å away.

In both the parallel displaced and sandwiched configurations, we noted that R- π appears in a location which corresponds to a real space separation larger than experiment. We attribute this discrepancy to GAFF's inability to appropriately model the aromatic interactions which would be necessary to achieve the

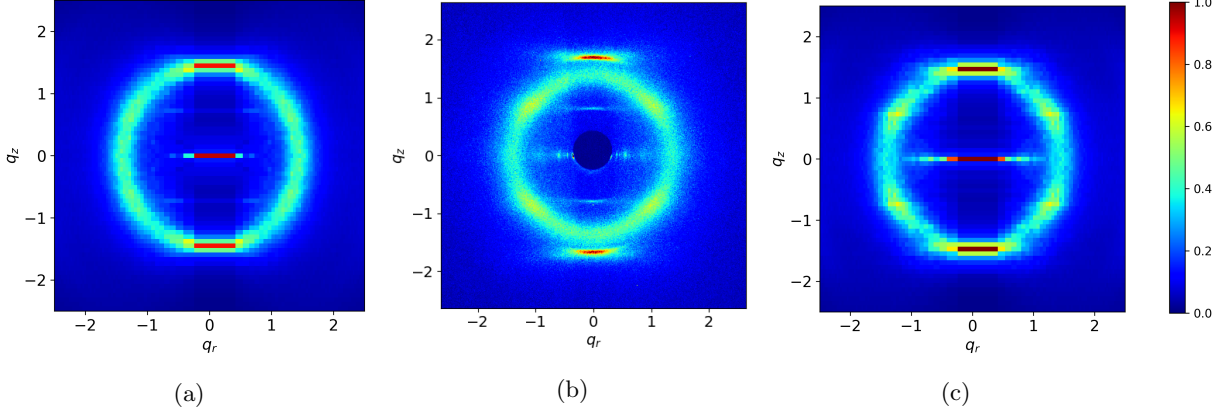


Figure 7: The simulated XRD pattern generated from the equilibrated trajectory of the parallel displaced configuration (a) exhibits all major reflections present in the experimental WAXS pattern (b). The simulated XRD pattern generated from the equilibrated trajectory in the sandwiched configuration shows all major reflections except R-helix.

correct π - π stacking distance. The system we have modeled has bulky tails whose entropic contributions compete with the π - π stacking interaction energy. There have been efforts to model systems that contain π interactions in a classical mechanical context using polarizable forcefields [40]. We could implement a polarizable force field, however it is likely not worth the extra computational cost. If our model proves to be inadequate when simulating transport, we will revisit our current choice of forcefield.

The R-spots signal, which appears in both simulated XRD patterns, is a result of hexagonal alkane chain packing. Previous literature has explained the spots in the diffraction pattern as the product of tilted alkane chains. We measured the tilt angle of the alkane chains and showed that our system equilibrates to an average tilt angle close to zero degrees (Fig. 8). To understand the origin of the spots, we determined which atoms gave rise to the feature. Since R-spots is present as higher intensity spots within R-alkanes, it is likely that the spots arise as a consequence of the tails. By removing all non-tail atoms from the trajectory and simulating a diffraction pattern, we were able to isolate the cause of the spots to the tails (Figure 9). Since the tails stay nearly flat, we plotted the centroids of the tails and measured the angle between each centroid and its nearest neighbors with respect to the plane of the membrane. We see distinct peaks in the distribution of these angles (Figure 10).

The peaks in the nearest neighbor angle distribution are consistent with the location of R-spots. The peaks of interest in Figures 10a and 10c are located at $\pm 33^\circ$ which is the same location where the highest intensity of spots are located on the simulated patterns. We confirmed this conclusion by radially integrating the 2D WAXS pattern for $|\mathbf{q}|$ values between 1.4 and 1.57 (between 4 and 4.5 Å in real space). We observe that distinct peaks appear ca. 30° , in close agreement with the previously measured angle distribution

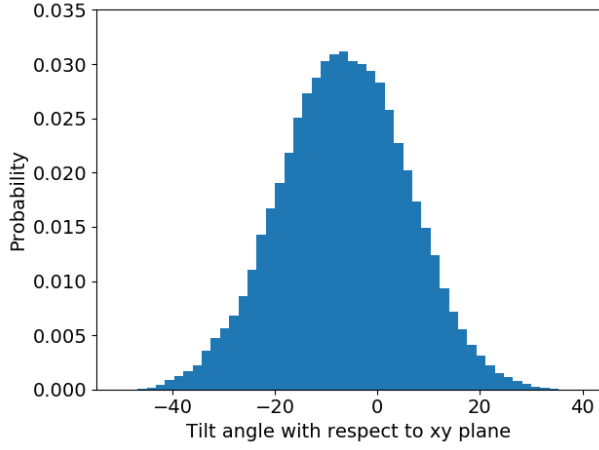


Figure 8: We measured the angle made between each monomer alkane tail and the membrane plane. The average tilt angle is near 7° which is far from the 37° tilt angle previously used to explain R-spots.

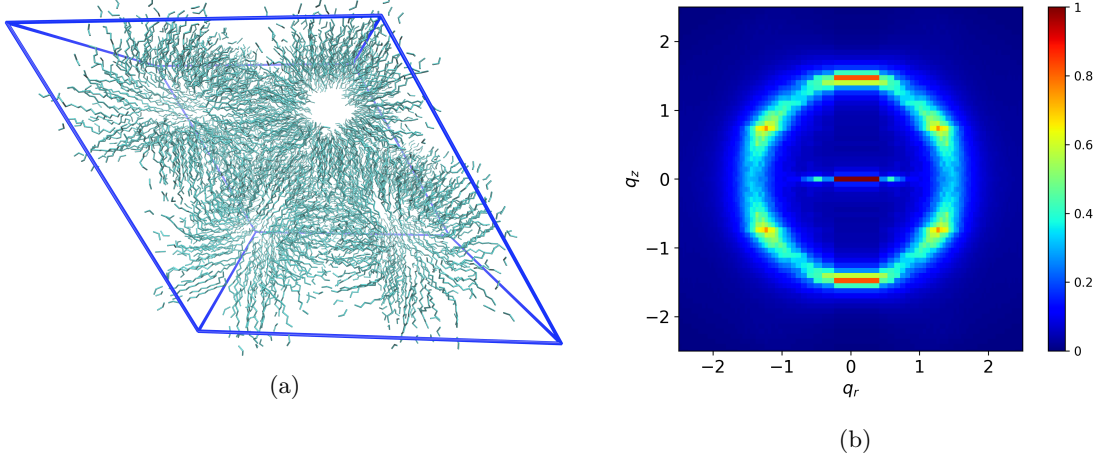


Figure 9: (a) We removed all atoms except carbon atoms that constitute the tails from a sandwiched configuration trajectory. (b) The simulated XRD pattern of the tail-only trajectory still shows R-spots

(Figs. 10b and 10d). We performed the same integration on the raw experimental data and found the angle at which R-spots reaches its highest intensity to be $\pm 37^\circ$ which is a reconcilable difference with our simulated results.

3.4 Initial Layer Spacing Affects System Equilibration

When we build systems with layers stacked 5.0 \AA apart and then let them equilibrate, we observe long-term stability of a qualitatively different configuration, suggesting that we have found another metastable free energy basin, further corroborating (4). For reasons to become apparent later, we will refer to this class of systems as the disordered pore basin. Systems which we build with layers initially stacked 3.7 \AA apart will

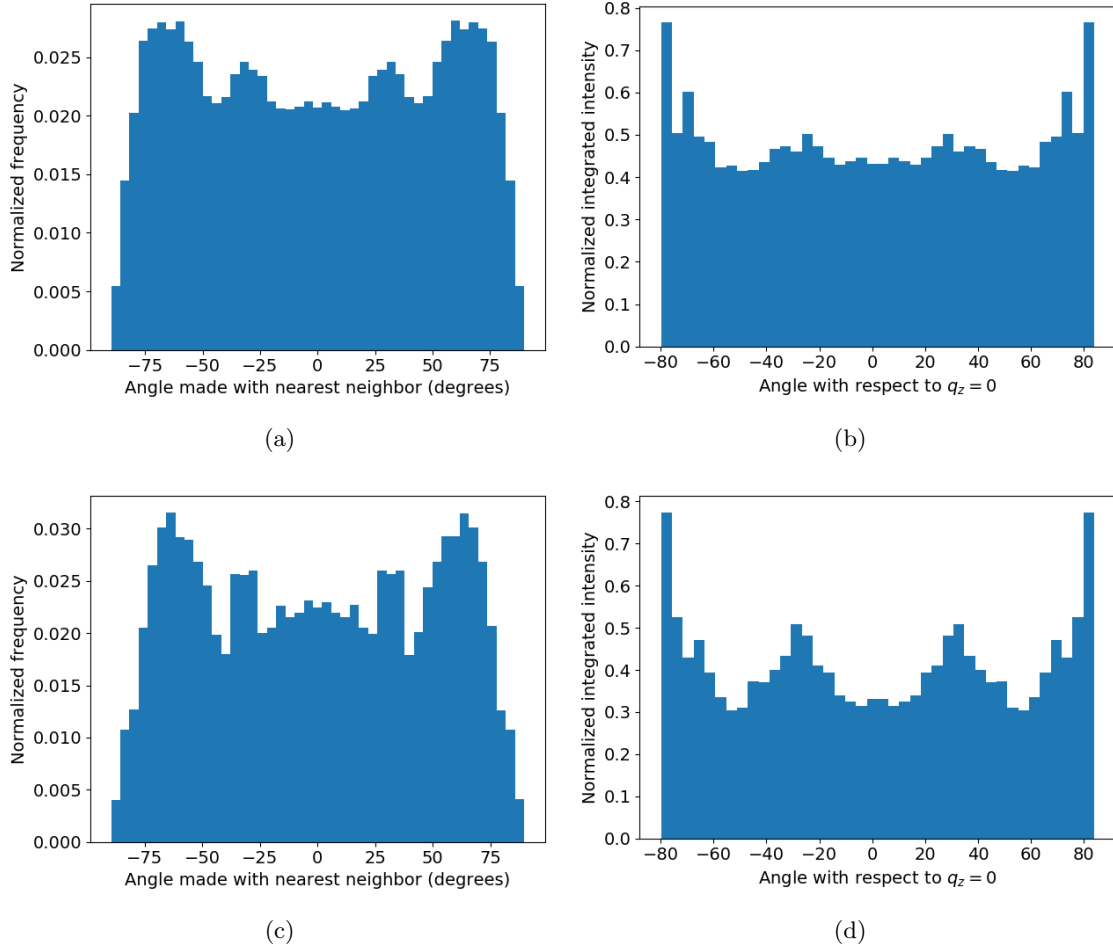


Figure 10: We hypothesize that R-spots is the result of ordered tail packing. Defining the membrane plane to be 0° , we measured the angles between each alkane chain tail centroid and its nearest neighbor centroids for the equilibrated parallel displaced (a) and sandwiched (c) configurations. Peaks that appear in each distribution are centered near $\pm 33^\circ$. We radially integrated the simulated XRD patterns of the parallel displaced and sandwiched configuration within the region bounding R-alkanes ((b) and (d) respectively). Peaks appear in the same location as the angle distributions which corroborates our hypothesis. Further, we note that the peaks are strongest in both plots associated with the sandwiched configuration. As shown in Figure 7c, systems simulated in the sandwiched configuration exhibit more intense R-spots reflections.

be referred to as the ordered basin. We studied each basin in both the parallel displaced and sandwiched configurations.

Structural properties are different in the disordered pore basin. In both configurations, we observe a decrease in pore spacing (Fig. 11b) and a corresponding increase in the equilibrated distance between layers (Fig. 11a). The simulated X-ray diffraction patterns indicate further structural differences. In the parallel displaced configuration, almost all contrast between R-spots and R-alkanes fades (Fig. 11c). In the sandwiched configuration, R-spots is weakly present, but in different locations, showing higher intensity at

the top and bottom of the pattern as well as at the intersection of R-alkanes with $q_z = 0$ (Fig. 11d).

The sandwiched and parallel displaced assemblies do not deviate from their initial head group arrangement. R-helix is still faintly visible in the parallel displaced configuration and is absent in the sandwiched simulated diffraction pattern. The spectroscopic signatures are unique to the two different head group configurations.

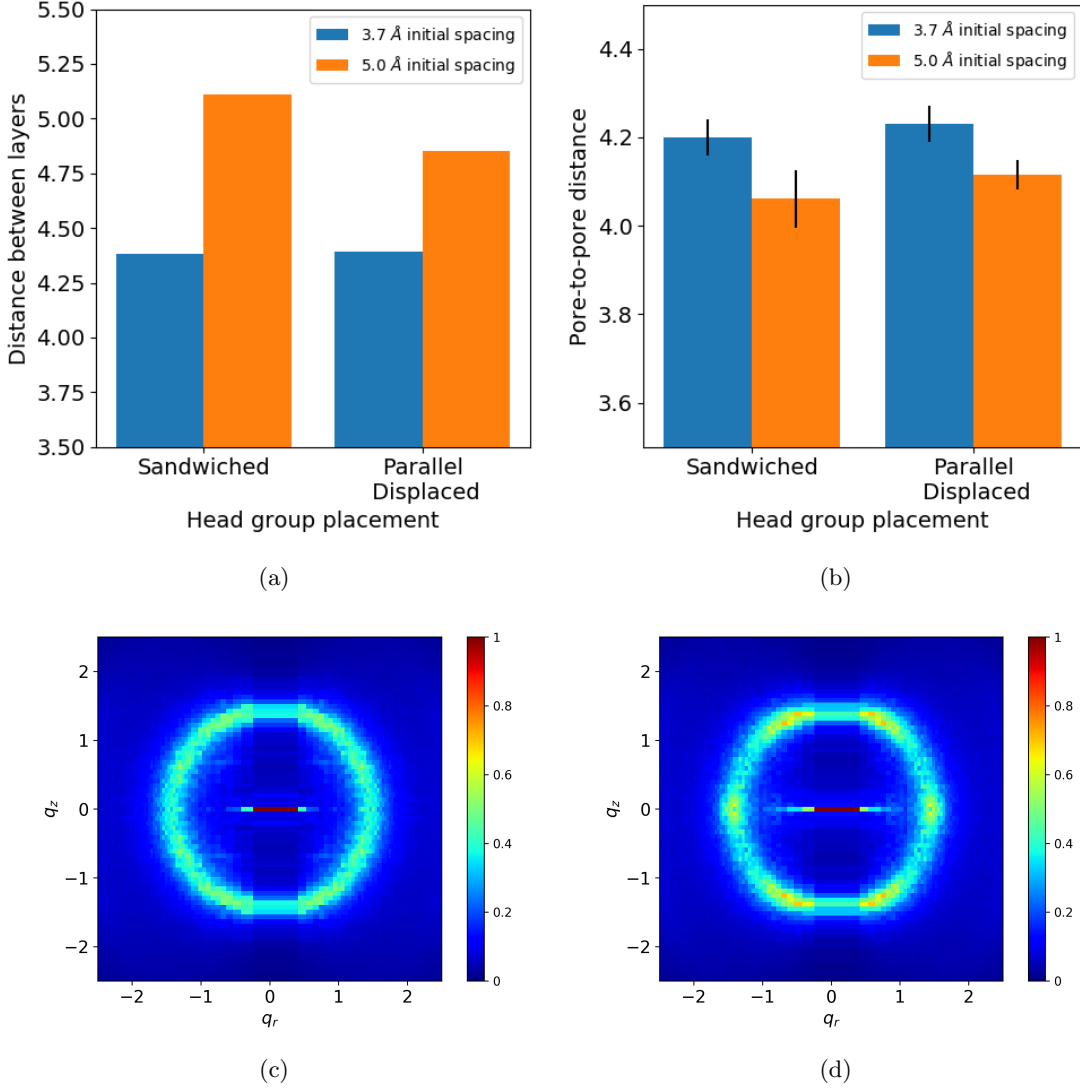


Figure 11: There are distinct differences between the disordered and ordered pore systems. When layers are initially stacked 5 Å apart, the distance between layers increases (a) and the pore spacing decreases (b) in comparison to the ordered pore systems. The simulated XRD patterns of disordered pore systems are also appreciably different, most notably in the region bounded by R-alkanes. The disordered pore systems started in the parallel displaced configuration (c) does not show R-spots or R- π which suggests that head groups are not associating with each other and tails are distributed nearly isotropically. The disordered pore system started in the sandwiched configuration (d) does not show R- π but R-spots are present in different locations because the tails are packed in a different motif.

3.5 Pore Structure Depends on Initial Configuration

In order to address (5), we plotted the number densities of heavy atoms in the head group, carbon atoms in the tail region and the sodium ions (Figure 12). For the head group region, we used the carbon atoms making up the aromatic ring. For the tail region we used only carbon atoms of the monomer tails (See Supplemental Information for diagram). We average the histograms over at least 50 ns of equilibrated trajectory.

In all cases, the space in the pore region is filled with sodium ions and head groups. In the ordered pore systems, there is less density in the center of the pore indicating a more ordered pore structure. In both the sandwich and parallel displaced configurations, we see the density of head groups and sodium ions fall to less than 50% of its maximum at $r = 0$ (Fig. 12b). The situation is most pronounced in the sandwiched configuration where the maximum head group density occurs 0.44 nm from the pore center. The parallel displaced configuration reaches its maximum 0.35 nm from the pore center. In contrast, both disordered pore systems show very little difference in density from its maximum. This implies a more uniform distribution of head groups within the pore center.

There is a partition between the hydrophobic and hydrophilic regions, however it is a gradient in composition, rather than an abrupt division. The system does not confine sodium ions and head groups to just within the pore region. Assuming a pore radius of 0.6 nm, we see in all cases, that 19% of sodium ions exist outside the pore region (except sandwiched, ordered pore , where 16% are outside the pore). Additionally, we see that in all cases, about 3% of the plotted tail density is located within the pore region (except sandwiched, ordered pore, where 1.5% are within the pore region). These observations bring into question how one should define a pore in these types of systems. One usually measures a membrane's pore radius based on the size of a molecule it can reject, however it is not clear where the edges of the pores are and what size molecule would fit through. We leave these investigations for a future study.

3.6 Affect of Water on Structure

We explored the affect of water on pore structure, addressing (6) by preparing parallel displaced and sandwiched configurations according to the wet equilibration procedure. There is no experimental measurement of trace water concentration in the pores so we tested a range of water concentrations from 0.5 to 5 percent. Our lower bound models a system with on average 2 water molecules for each monomer layer. Figure 13 shows the simulated diffraction patterns resulting from each configuration.

In all cases, water disrupts structuring of the model 13. When we add water to the system, the intensity of the reflections decrease. In systems built with 5 wt% water, R- π and R-spots become nearly indistinguishable from R-alkanes.

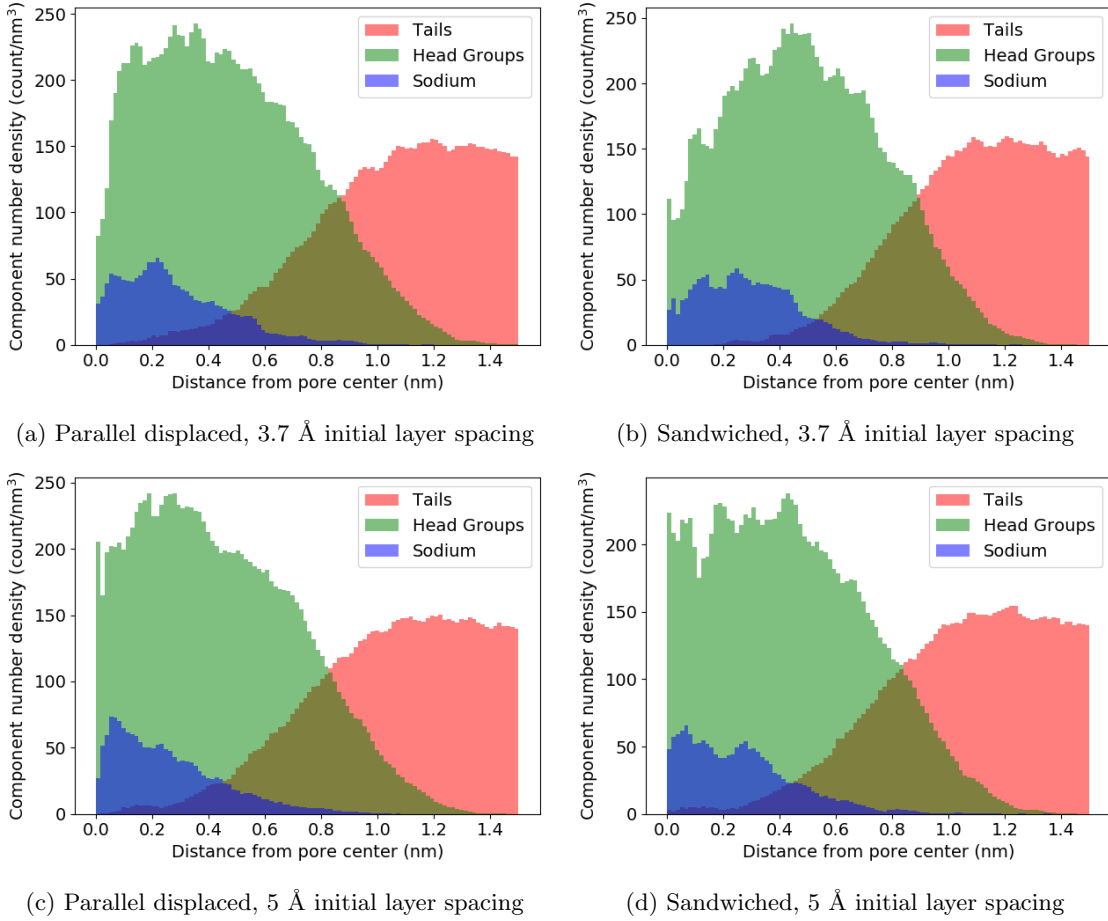


Figure 12: In all cases, the component radial distribution functions exhibit a composition gradient transitioning from the hydrophilic to the hydrophobic regions. Systems with layers initially spaced 3.7 Å apart in the parallel displaced (a), and sandwiched (b) configurations both show the highest concentrations of ions and head groups away from the pore center. Systems with layers initially spaced 5 Å apart (c) and (d), both show the highest concentrations of ions and head groups near the pore center, implying a more uniform, disordered pore.

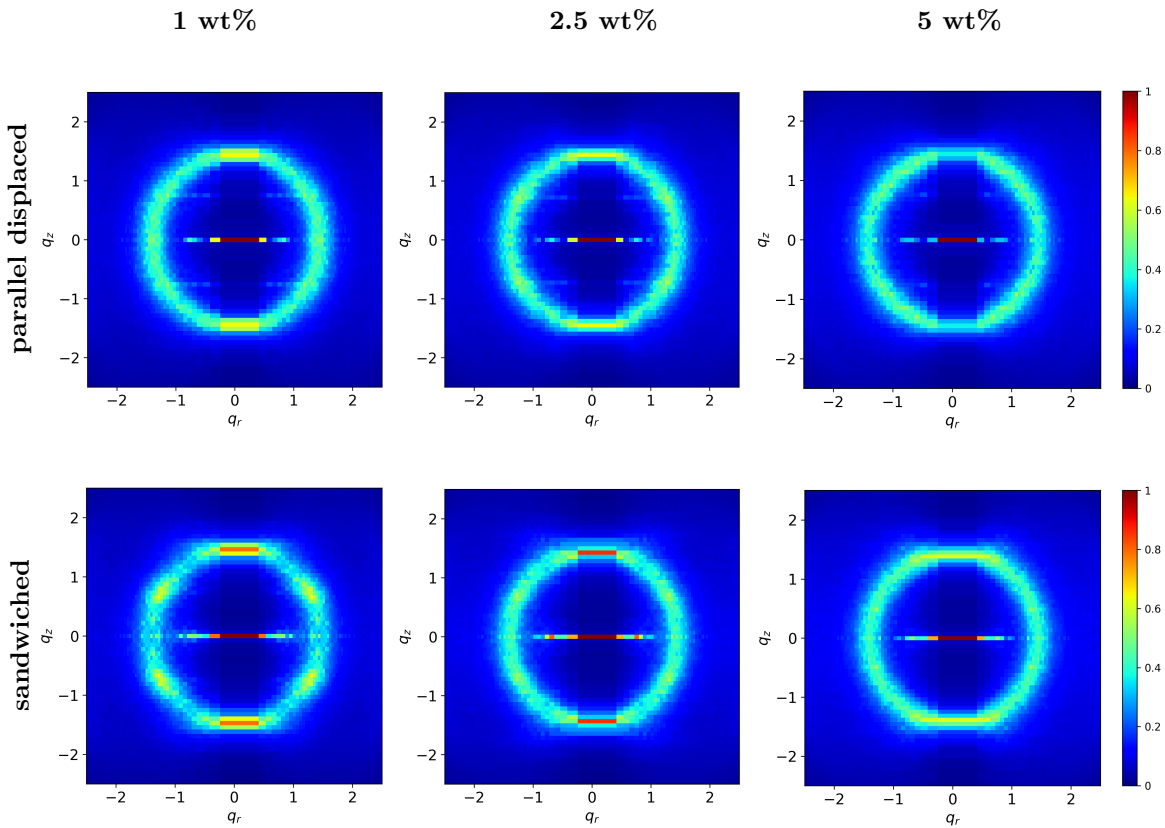


Figure 13: Simulated diffraction patterns generated from trajectories of systems built in the parallel displaced and sandwiched configurations as a function of water content shows weaker reflections than the dry system.

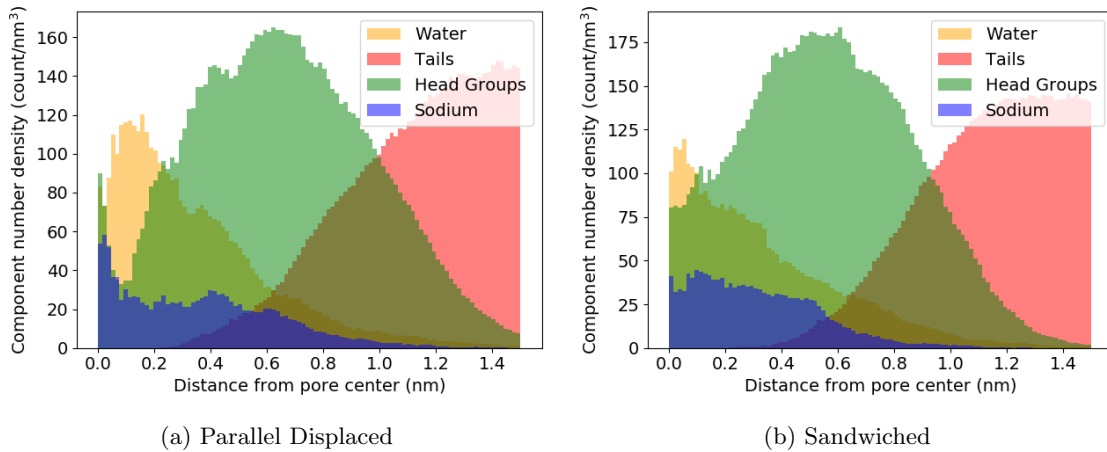


Figure 14: Water fills the membrane pores in the parallel displaced (a) and sandwiched (b) configurations. Sodium ions are distributed fairly uniformly within the pore region, defined by a radius of 0.6 nm.

Water is not necessary to maintain an ordered pore structure. We do not eliminate the possibility that water is necessary in order to drive self-assembly, but studying the mechanisms of self-assembly is beyond the scope of this work. According to our model, once the system has formed the Col_h phase, adding water only drives disorder of the pore structure. In the true equilibrium configuration, if water exists, it is primarily confined to the pore region where there is no driving force for aggregation of water molecules. In the case of trace water, water molecules will be too sparse to form a hydrogen bonding network.

In systems built with 5 wt% water, the pore region becomes filled with water. We plotted the number density of components in this system. As with the dry systems, we see a gradual compositional transition from hydrophilic to hydrophobic. We see that the pores become a mixture of water molecules and sodium ions (Fig. 14).

The membrane swells when we introduce water. The location of maximum head group density shifts from 0.35 to 0.62 nm and from 0.44 to 0.61 nm in the parallel displaced and sandwiched configurations respectively. Again, we observe the existence of ions, head groups and water outside the pore region, however in the hydrated system, the head groups drift beyond 1.5 Å from the pore center. In the dry systems, head groups did not wander beyond 1.4 Å from the pore center. Both observations suggest that water pushes all components radially outward from the pore center, characteristic of a swelling process.

This system is a closer representation of the H_{II} phase which is typically synthesized with ca. 8 wt% water. Further investigation of hydrated systems can help unravel the mechanisms for selective transport in separations of aqueous solutions.

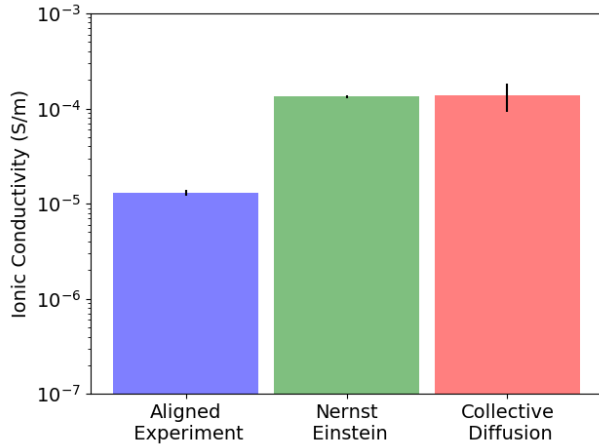


Figure 15: Calculated ionic conductivity using the Nernst-Einstein relation and Collective Diffusion model agree with error. Both methods give calculated values of ionic conductivity an order of magnitude higher than the experimental value.

3.7 Model Ionic Conductivity Measurements

We used the equilibrated parallel displaced system to calculate ionic conductivity since its structure is the closest match to experiment. The model gives reasonable estimates of ionic conductivity when compared to experiment. We compare calculated values of ionic conductivity obtained using the Nernst-Einstein relation and Collective Diffusion model in Figure 15. The two methods agree with each other within error, although the uncertainty obtained using the Collective Diffusion model is much higher. We require much longer simulations to lower the uncertainty, however it is not feasible to do so with a large system. We will only use the Nernst-Einstein relation in future calculations of this type.

The calculated values of ionic conductivity are higher than experiment by an order of magnitude. One can justify the reason for this result by considering the real system studied experimentally. The ionic conductivity measurement to which we are comparing was done with a 80 μm thick film, nearly 10,000 times thicker than our simulated system. The thick film is likely imperfectly aligned and has defects leading to non-contiguous pores. It has been shown that there is a large dependence of ionic conductivity on the alignment of the pores. The ionic conductivity of an unaligned film is ca. 85 times lower than that of a nearly aligned film referenced here. We hypothesize that a thin, perfectly aligned film would have a value of ionic conductivity in closer agreement with our model.

3.8 Effect of Crosslinking

The system's structure and physical characteristics did not change significantly when we applied the cross-linking algorithm to the equilibrated parallel-displaced configuration built with 5 monomers per layer. We

simulated the cross-linked system in the NPT ensemble for 100 ns. After the system is cross-linked, the distance between pores shrinks by 0.4 Å and the distance between layers increases by 0.04 Å. All major features are still present in the simulated XRD patterns, however at lower intensities (Fig. 16a). We calculated the ionic conductivity using the Nernst-Einstein relation and found that it is lower in the cross-linked system (Fig. 16b).

4 Conclusion

We have used a detailed molecular model of the Col_h phase formed by Na-GA3C11 in order to study its nanoscopic structure. While there have been efforts to model formation of various liquid crystalline phases with molecular dynamics, to our knowledge there have been no studies which attempt to examine their structure with the same level of detail presented here.

Evidence strongly supports that monomers stay partitioned into layers which stack to create pores and that each layer contains 5 monomers. We see periodic spacing of layers based on the z-direction correlation function, $g(z)$ of atoms in the tails and separately of atoms in the head groups. Systems not built with 5 monomers per layer result in assemblies whose pore-to-pore spacing is inconsistent with experiment.

We have explored the affect of two different π - π stacking modes on the equilibrated membrane structure. Simulated diffraction patterns generated from MD trajectories suggest that the parallel-displaced configuration produces a structure with the closest match to experiment.

We have observed a number of metastable configurations. We witnessed long-term stability of systems built with a varied number of monomers per layer as well as in different π - π stacking configurations. We also examined how the structure changes based on the initial distance between layers and showed how systems differ when built with layers spaced 5 Å versus 3.7 Å apart. The configuration that showed the greatest agreement with experiment was built in the parallel-displaced configuration, with 5 monomers per layer and an initial layer spacing of 3.7 Å.

We characterized the environment centered around the membrane pores and learned that the pores are generally filled by monomer head groups and sodium ions. Membranes prepared in the sandwiched configuration have lower density pores. We also observed that there is not a hard partition between hydrophobic and hydrophilic regions, rather there is a gradient. This finding has raised questions about the nature of any size-exclusion separations.

We learned that we do not need water to create well-defined pore structures. Systems whose pores were filled with varying amounts of water showed a decrease in structuring relative to dry systems.

We justified that our system can reasonably estimate ionic conductivity. Our calculations are about

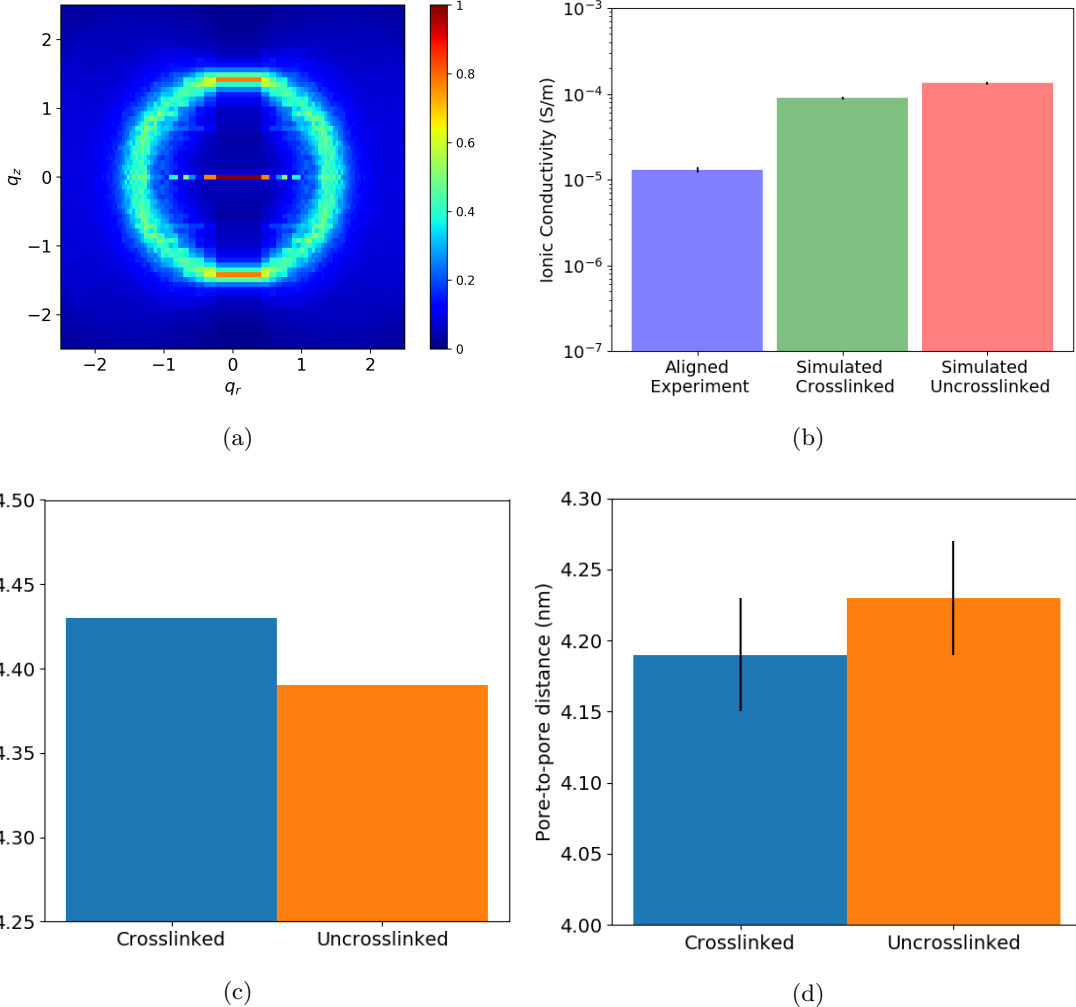


Figure 16: (a) Reflections produced by the cross-linked configuration fade relative to the uncross-linked system. The colorbar shown is the same used for the uncross-linked system. (b) The ionic conductivity is smaller relative to the uncross-linked system, but still much larger than the experimental value. When the system is cross-linked, The distance between layers increases (c) and the pore spacing decreases (d)

1 order of magnitude higher than experiment, however that is to be expected since we are simulating a perfectly straight and defect-free membrane.

Finally, we verified that our conclusions do not change when the system is cross-linked by the algorithm we implemented. The diffraction pattern weakens relative to the uncross-linked system, the ionic conductivity drops by a factor of ca. 1.5, in closer agreement with experiment, the pore spacing decreases and the membrane becomes thicker.

With the structural understanding gained by these simulations, we will evaluate transport of various solutes within the system. We will apply the knowledge gained from this study in order to suggest improvements to the existing system as well as to evaluate new unsynthesized LLC systems.

References

- [1] T. Humplik, J. Lee, S. C. OHern, B. A. Fellman, M. A. Baig, S. F. Hassan, M. A. Atieh, F. Rahman, T. Laoui, R. Karnik, and E. N. Wang, “Nanostructured materials for water desalination,” *Nanotechnology*, vol. 22, no. 29, p. 292001, 2011.
- [2] B. Van Der Bruggen, C. Vandecasteele, T. Van Gestel, W. Doyen, and R. Leysen, “A review of pressure-driven membrane processes in wastewater treatment and drinking water production,” *Environ. Prog.*, vol. 22, pp. 46–56, Apr. 2003.
- [3] J. R. Werber, C. O. Osuji, and M. Elimelech, “Materials for next-generation desalination and water purification membranes,” *Nature Reviews Materials*, vol. 1, p. 16018, May 2016.
- [4] B.-H. Jeong, E. M. V. Hoek, Y. Yan, A. Subramani, X. Huang, G. Hurwitz, A. K. Ghosh, and A. Jawor, “Interfacial polymerization of thin film nanocomposites: A new concept for reverse osmosis membranes,” *Journal of Membrane Science*, vol. 294, pp. 1–7, May 2007.
- [5] C. A. Smolders, A. J. Reuvers, R. M. Boom, and I. M. Wienk, “Microstructures in phase-inversion membranes. Part 1. Formation of macrovoids,” *Journal of Membrane Science*, vol. 73, pp. 259–275, Oct. 1992.
- [6] P. Apel, “Track etching technique in membrane technology,” *Radiation Measurements*, vol. 34, pp. 559–566, June 2001.
- [7] D. Cohen-Tanugi, L.-C. Lin, and J. Grossman, “Multilayer Nanoporous Graphene Membranes for Water Desalination,” *Nano Lett.*, vol. 16, pp. 1027–1033, Jan. 2016.
- [8] K. Hata, D. N. Futaba, K. Mizuno, T. Namai, M. Yumura, and S. Iijima, “Water-Assisted Highly Efficient Synthesis of Impurity-Free Single-Walled Carbon Nanotubes,” *Science*, vol. 306, pp. 1362–1364, Nov. 2004.
- [9] S. Maruyama, E. Einarsson, Y. Murakami, and T. Edamura, “Growth process of vertically aligned single-walled carbon nanotubes,” *Chemical Physics Letters*, vol. 403, pp. 320–323, Feb. 2005.
- [10] S. MURAD, K. ODER, and J. LIN, “Molecular simulation of osmosis, reverse osmosis, and electroosmosis in aqueous and methanolic electrolyte solutions,” *Molecular Physics*, vol. 95, pp. 401–408, Oct. 1998.
- [11] L. Li, J. Dong, T. M. Nenoff, and R. Lee, “Desalination by reverse osmosis using MFI zeolite membranes,” *Journal of Membrane Science*, vol. 243, pp. 401–404, Nov. 2004.

- [12] X. Feng, M. E. Tousley, M. G. Cowan, B. R. Wiesnauer, S. Nejati, Y. Choo, R. D. Noble, M. Elimelech, D. L. Gin, and C. O. Osuji, “Scalable Fabrication of Polymer Membranes with Vertically Aligned 1 nm Pores by Magnetic Field Directed Self-Assembly,” *ACS Nano*, vol. 8, pp. 11977–11986, Dec. 2014.
- [13] R. C. Smith, W. M. Fischer, and D. L. Gin, “Ordered Poly(p-phenylenevinylene) Matrix Nanocomposites via Lyotropic Liquid-Crystalline Monomers,” *Journal of the American Chemical Society*, vol. 119, no. 17, pp. 4092–4093, 1997.
- [14] M. Zhou, T. J. Kidd, R. D. Noble, and D. L. Gin, “Supported Lyotropic Liquid-Crystal Polymer Membranes: Promising Materials for Molecular-Size-Selective Aqueous Nanofiltration,” *Adv. Mater.*, vol. 17, pp. 1850–1853, Aug. 2005.
- [15] R. Resel, U. Theissl, C. Gadermaier, E. Zojer, M. Kriechbaum, H. Amenitsch, D. Gin, R. Smith, and G. Leising, “The H₂-phase of the lyotropic liquid crystal sodium 3,4,5-tris(omega-acryloyloxyundecyloxy)benzoate,” *Liquid Crystals*, vol. 27, pp. 407–411, Mar. 2000.
- [16] X. Feng, S. Nejati, M. G. Cowan, M. E. Tousley, B. R. Wiesnauer, R. D. Noble, M. Elimelech, D. L. Gin, and C. O. Osuji, “Thin Polymer Films with Continuous Vertically Aligned 1 nm Pores Fabricated by Soft Confinement,” *ACS Nano*, vol. 10, pp. 150–158, Jan. 2016.
- [17] R. Resel, G. Leising, P. Markart, M. Kriechbaum, R. Smith, and D. Gin, “Structural properties of polymerised lyotropic liquid crystals phases of 3,4,5-tris(\$mega\$-acryloxyalkoxy)benzoate salts,” *Macromolecular Chemistry and Physics*, vol. 201, no. 11, pp. 1128–1133, 2000.
- [18] E. S. Hatakeyama, C. J. Gabriel, B. R. Wiesnauer, J. L. Lohr, M. Zhou, R. D. Noble, and D. L. Gin, “Water filtration performance of a lyotropic liquid crystal polymer membrane with uniform, sub-1-nm pores,” *Journal of Membrane Science*, vol. 366, no. 1-2, pp. 62–72, 2011.
- [19] X. Zhu, M. A. Scherbina, A. V. Bakirov, B. Gorzolnik, S. N. Chvalun, U. Beginn, and M. Mller, “Methacrylated Self-Organizing 2,3,4-Tris(alkoxy)benzenesulfonate: A New Concept Toward Ion-Selective Membranes,” *Chem. Mater.*, vol. 18, pp. 4667–4673, Sept. 2006.
- [20] E. Gazit, “A possible role for -stacking in the self-assembly of amyloid fibrils,” *FASEB J*, vol. 16, pp. 77–83, Jan. 2002.
- [21] M. O. Sinnokrot, E. F. Valeev, and C. D. Sherrill, “Estimates of the Ab Initio Limit for Interactions: The Benzene Dimer,” *J. Am. Chem. Soc.*, vol. 124, pp. 10887–10893, Sept. 2002.

- [22] M. P. Waller, A. Robertazzi, J. A. Platts, D. E. Hibbs, and P. A. Williams, “Hybrid density functional theory for -stacking interactions: Application to benzenes, pyridines, and DNA bases,” *J. Comput. Chem.*, vol. 27, pp. 491–504, Mar. 2006.
- [23] A. L. Ringer, M. O. Sinnokrot, R. P. Lively, and C. D. Sherrill, “The Effect of Multiple Substituents on Sandwich and T-Shaped Interactions,” *Chem. Eur. J.*, vol. 12, pp. 3821–3828, May 2006.
- [24] T. J. McIntosh, S. A. Simon, and R. C. MacDonald, “The organization of n-alkanes in lipid bilayers,” *Biochimica et Biophysica Acta (BBA) - Biomembranes*, vol. 597, pp. 445–463, Apr. 1980.
- [25] A. S. Govind and N. V. Madhusudana, “A simple molecular theory of smectic-C liquid crystals,” *EPL*, vol. 55, p. 505, Aug. 2001.
- [26] J. Wang, R. M. Wolf, J. W. Caldwell, P. A. Kollman, and D. A. Case, “Development and testing of a general amber force field,” *J. Comput. Chem.*, vol. 25, pp. 1157–1174, July 2004.
- [27] J. Wang, W. Wang, P. A. Kollman, and D. A. Case, “Automatic atom type and bond type perception in molecular mechanical calculations,” *Journal of Molecular Graphics and Modelling*, vol. 25, pp. 247–260, Oct. 2006.
- [28] D. Case, R. Betz, W. Botello-Smith, D. Cerutti, T. Cheatham, III, T. Darden, R. Duke, T. Giese, H. Gohlke, A. Goetz, N. Homeyer, S. Izadi, P. Janowski, J. Kaus, A. Kovalenko, T. Lee, S. LeGrand, P. Li, C. Lin, T. Luchko, R. Luo, B. Madej, D. Mermelstein, K. Merz, G. Monard, H. Nguyen, H. Nguyen, I. Omelyan, A. Onufriev, D. Roe, A. Roitberg, C. Sagui, C. Simmerling, J. Swails, R. Walker, J. Wang, R. Wolf, X. Wu, L. Xiao, D. York, and P. Kollman, “AmberTools16,” Apr. 2016.
- [29] H. Bekker, H. J. C. Berendsen, E. J. Dijkstra, S. Achterop, R. van Drunen, D. van der Spoel, A. Sijsbers, H. Keegstra, B. Reitsma, and M. K. R. Renardus, “Gromacs: A parallel computer for molecular dynamics simulations,” *Physics Computing*, 1993.
- [30] H. J. C. Berendsen, D. van der Spoel, and R. van Drunen, “GROMACS: A message-passing parallel molecular dynamics implementation,” *Computer Physics Communications*, vol. 91, pp. 43–56, Sept. 1995.
- [31] D. Van Der Spoel, E. Lindahl, B. Hess, G. Groenhof, A. E. Mark, and H. J. C. Berendsen, “GROMACS: Fast, flexible, and free,” *J. Comput. Chem.*, vol. 26, pp. 1701–1718, Dec. 2005.
- [32] B. Hess, C. Kutzner, D. van der Spoel, and E. Lindahl, “GROMACS 4: Algorithms for Highly Efficient, Load-Balanced, and Scalable Molecular Simulation,” *J. Chem. Theory Comput.*, vol. 4, pp. 435–447, Mar. 2008.

- [33] J. Mondal, M. Mahanthappa, and A. Yethiraj, “Self-Assembly of Gemini Surfactants: A Computer Simulation Study,” *J. Phys. Chem. B*, vol. 117, pp. 4254–4262, Apr. 2013.
- [34] L. Martnez, R. Andrade, E. G. Birgin, and J. M. Martnez, “PACKMOL: A package for building initial configurations for molecular dynamics simulations,” *J. Comput. Chem.*, vol. 30, pp. 2157–2164, Oct. 2009.
- [35] R. Young and P. Lovell, *Introduction to Polymers*. CRC Press, 3 ed., 2011.
- [36] J. D. Chodera, “A Simple Method for Automated Equilibration Detection in Molecular Simulations,” *Journal of Chemical Theory and Computation*, vol. 12, pp. 1799–1805, Jan. 2016.
- [37] M. R. Shirts and J. D. Chodera, “Statistically optimal analysis of samples from multiple equilibrium states,” *The Journal of Chemical Physics*, vol. 129, p. 124105, Sept. 2008.
- [38] A. Einstein, “Investigations on the theory of the brownian movement,” *Dover Publications*, 1956.
- [39] Y. Liu and F. Zhu, “Collective diffusion model for ion conduction through microscopic channels,” *Biophys. J.*, vol. 104, pp. 368–376, Jan. 2013.
- [40] C. M. Baker, “Polarizable force fields for molecular dynamics simulations of biomolecules,” *WIREs Comput Mol Sci*, vol. 5, pp. 241–254, Mar. 2015.